



Supplementary Materials for

Enhanced Role of Transition Metal Ion Catalysis During In-Cloud Oxidation of SO₂

Eliza Harris,* Bärbel Sinha,* Dominik van Pinxteren, Andreas Tilgner,
Khanneh Wadinga Fomba, Johannes Schneider, Anja Roth, Thomas Gnauk,
Benjamin Fahlbusch, Stephan Mertes, Taehyoung Lee, Jeffrey Collett, Stephen Foley,
Stephan Borrmann, Peter Hoppe, Hartmut Herrmann

*Corresponding author. E-mail: elizah@mit.edu (E.H.); baerbel.sinha@mpic.de (B.S.)

Published 10 May 2013, *Science* **340**, 727 (2013)

DOI: 10.1126/science.1230911

This PDF file includes:

Texts S1 and S2

Figs. S1 to S5

Tables S1 to S10

References

S1.1 Description of site and measurement periods

The field measurements for HCCT-2010 were carried out in the Thüringer Wald, central Germany, in Autumn, 2010. The in-cloud measurement station is located at the Umweltbundesamt (Federal Environment Agency) mountain station ‘Schmücke’ (937 m asl). The upwind station ‘Goldlauter’ (605 m asl) is located around 3 km southwest of Schmücke and the downwind station ‘Gehlberg’ (732 m asl) is around 3 km to the northeast of Schmücke. Southwesterly winds cause air parcels to pass through the three stations in series, while crossing a low mountain ridge which extends for around 60 km in a south-east to north-west direction, often resulting in orographic cloud formation at Schmücke as air parcels are lifted.

Cloud measurements were taken when the following conditions were met: Liquid water content (LWC) $> 0.1 \text{ g m}^{-3}$, wind direction between 200° and 250° , wind speed between 2 and 12 m s^{-1} , valley stations free of fog and all sites free of precipitation, and temperature $> 0^\circ\text{C}$. Samples for sulfur isotope analysis were collected during three cloud events and one cloud-free period (Table S2). Comparing the HYSPLIT (NOAA Air Resources Laboratory) back trajectories for the three cloud events with the SO_2 emission strength [1] showed that air masses in FCE 11.2 and FCE 11.3 had passed more recently over strong emission sources in eastern Europe than air masses in FCE 7.1 or NC 1, explaining the higher SO_2 concentrations.

S1.2 Connected flow analysis

With regard to the connected flow conditions between the sites, all measurement periods were investigated using ozone concentration profiles, ozone cross-correlations and hydrodynamic flow analysis [2, 3]. Furthermore, the coefficient of deviation (COD) for several aerosol particle bins and for ozone concentrations were calculated in order to characterise the connected flow conditions. Connected flow between the sites was also occasionally measured with tracer experiments following the release of an inert gas (SF_6) at Goldlauter. SF_6 was measured in

air samples taken at 5-minute intervals at various sites downwind of Goldlauter, including the in-cloud measurement site Schmücke and the downwind measurement site Gehlberg.

FCE 7.1 was relatively short and only showed connected flow conditions for half of the event. FCE 11.2 and FCE 11.3 had good connected flow conditions during the whole event duration. The coefficient of deviation (COD) for ozone concentration between the three measurement sites was low for all three events, which showed that flow was at least partially connected during all three measurement periods. The connected flow analyses will be discussed in detail in a forthcoming paper in the HCCT special issue of *Atmospheric Chemistry and Physics*.

S1.3 Sample collection

SO₂ and sulfuric acid gases were collected for isotopic analysis at the upwind and downwind sites according to the methods presented in [4]. Particulate samples were collected on filter packs at all three measurement stations, however they were not collected during FCE 7.1 due to equipment problems. At the in-cloud measurement site, cloud droplet residuals (particulate matter from evaporated cloud droplets, ie. those particles that were activated in the cloud) and interstitial (non-activated) particles were collected separately with a counterflow virtual impactor (CVI) and a complementary droplet-segregating interstitial inlet (INT) [5, 6]. The system had an operationally-defined discrimination diameter of 5 μm for separation of the two aerosol populations.

Nuclepore track-etch polycarbonate membrane filters (Whatman Ltd.) with 5 and 0.2 μm pores for coarse and fine particulate respectively, which had been coated with a 10 nm-thick gold layer using a sputter coater (Bal-tec GmbH, Model SCD-050) prior to sample collection, were used to collect particulate samples. The SEM-measured lower cut-off diameter was ~ 50 nm for the fine particles, and the effective cut-off between the coarse and fine filters was around 600 nm, with tails in both directions caused by the random distribution of pores across the filter

and variations in particle density and shape. Whenever only particles $< 1 \mu\text{m}$ were encountered for a particular particle type in a particular sample, particles on both filters were combined and classified as fine. For particle classes where both “coarse” ($> 1 \mu\text{m}$) and “fine” ($< 1 \mu\text{m}$) particles were encountered in a given sample, the fine and coarse filters were used as a guide to the size-dependency of different processes (S2.2). The cut-off does not conform exactly to the traditional definitions of coarse particles $> 1 \mu\text{m}$ > fine particles.

S1.4 Stable sulfur isotope analysis of gas-phase and particulate sulfur

The sulfur isotopic composition of the particles was determined with the Cameca NanoSIMS 50 ion probe at the Max Planck Institute for Chemistry in Mainz [7, 8]. The use of this instrument to analyse sulfur isotope ratios is described in detail in [9] and [10] and analysis conditions similar to those used for the current study are given in [4], so only a brief description of differences to the previous method will be included here. The samples were analysed directly on the gold-coated filters without further processing. For particulate samples secondary ions of $^{16}\text{O}^-$, $^{12}\text{C}_2^-$, $^{26}\text{CN}^-$, $^{32}\text{S}^-$ and $^{34}\text{S}^-$ were measured. For the BaSO_4 samples of gas-phase sulfur, some samples were measured for secondary ions of $^{16}\text{O}^-$, $^{12}\text{C}_2^-$, $^{26}\text{CN}^-$, $^{32}\text{S}^-$ and $^{34}\text{S}^-$ and some for $^{16}\text{O}^-$, $^{32}\text{S}^-$, $^{33}\text{S}^-$, $^{34}\text{S}^-$ and $^{36}\text{S}^-$. In both cases the $^{34}\text{S}/^{32}\text{S}$ ratio was measured with equal precision. Presputtering was carried out on an area $\geq 10 \mu\text{m} \times 10 \mu\text{m}$ to conserve sulfate for analysis. Analyses were terminated as soon as all the particles had been sputtered away, therefore the number of cycles per analysis was variable.

The instrumental mass fractionation (IMF) correction in each measurement session was determined with the commercially available BaSO_4 isotope standards IAEA-SO5 and IAEA-SO6. The matrix-specific IMF corrections relative to BaSO_4 [10] were used to correct for matrix-dependent IMF on the different particle types. Secondary organic aerosol (SOA) particles containing inorganic salts (mixed particles) with an O/S ratio measured in the NanoSIMS of < 2

were considered to be predominantly ‘organic’ and were corrected with the IMF for cysteine ($-13.5 \pm 1.7\%$ relative to BaSO_4). The most abundant cations in ‘inorganic’ mixed particles ($\text{O/S} > 3$) were found from the SEM-EDX analysis to be Na^+ and K^+ , so these particles were corrected by weighting the individual IMFs for Na^+ and K^+ by their abundances ($-8.4 \pm 2.7\%$ relative to BaSO_4). Mixed particles with an O/S ratio between 2 and 3 were corrected by assuming they consisted of a mixture of organic and inorganic sulfates, thus the average IMF for organic and inorganic mixed particles of $-11.2 \pm 3.2\%$ relative to BaSO_4 was used. Coated soot particles were corrected for matrix-dependent IMF in the same manner as the mixed particles. Chlorine was enriched on the mineral dust particle surfaces, suggesting the presence of condensed salts, which could supply cations to form sulfate salts. The cations within the dust are likely to be tightly bound and not available to influence sulfate ionisation. As with the inorganic mixed particles, Na^+ and K^+ were found to be the most important cations and the abundance-weighted IMF was used ($-8.4 \pm 2.7\%$ relative to BaSO_4). The error in the matrix-specific IMF was added to the counting statistical error, and the overall error for each individual particle was typically 7-8%.

S1.5 Analysis of cloud water TMI concentrations

TMIs were measured in bulk cloud water, which was collected using a Caltech Active Strand Cloud Water Collector [11] with an hourly sampling routine. 1 ml of cloud water was filtered through an $0.45 \mu\text{m}$ filter, and 0.5 ml of the filtrate was then used for TMI determination with an ion chromatograph (IC, Dionex ICS 900). The following TMIs were detected simultaneously at 530 nm using a variable wavelength UV/VIS detector: Fe^{3+} , Cu^{2+} , Ni^{2+} , Zn^{2+} , Cd^{2+} , Co^{2+} , Mn^{2+} , and Fe^{2+} . The ions were identified from their respective retention times on the chromatogram. Quantification was done via external calibration and blank values were subtracted from the measurements. The detection limit of the iron species was about $0.1 \mu\text{M}$. Most other

metals had similar detection limits to the iron species, except Ni^{2+} and Cd^{2+} , which had a detection limit 70-80% higher. Several ions that could be very active in catalysing SO_2 oxidation, such as Ti and Cr, were unfortunately not measured in cloud water as dissolved ions by ion chromatography during HCCT. Previous laboratory results have shown that these metals can be leached in catalytically-active quantities from natural dust [12]. A wider range of metals were measured in impactor samples at the at the upwind and downwind stations with a total reflection x-ray fluorescence (TXRF) technique [13]. However, these results show the total and not the soluble metal ion concentration and can only provide a guide to the potential cloud water concentrations of the different species. These ions can also be present in multiple oxidation states, which could further effect the catalysis rate.

S1.6 Other measurements

S1.6.1 Trace gases: SO_2 concentration was measured with a time resolution of one minute using a Thermo Environmental trace level pulsed fluorescence SO_2 analyser (model TE43C-TL) at Gehlberg and Goldlauter and an MLU (Monitoring für Leben und Umwelt) enhanced trace level SO_2 analyzer (model 43i-) at Schmücke. O_3 concentration was measured with a time resolution of one minute using a Thermo Environmental U.V. Photometric Gas Analyzer (model TE49C-TL) at Gehlberg and Goldlauter and a Horiba Ambient Ozone Monitor (model APOA 360) at Schmücke.

S1.6.2 Cloud water: Cloud water was collected as detailed in S1.5. H_2O_2 in cloud water is preserved on site with *p*-hydroxyphenylacetic acid (POPHA) to form a stable dimer; potassium hydrogen phthalate and EDTA are also added to buffer the solution and prevent interferences from metal ions. The POPHA- H_2O_2 dimer is later measured quantitatively with a fluorescence

spectrophotometer [14, 15]. The LWC was measured by a particle volume monitor (PVM-100, Gerber Scientific, USA) [16, 17].

SI.6.3 Water soluble compounds: Water-soluble gases and particles at the upwind site were measured with MARGA (Monitor for AeRosols and Gases in Air). Gases are collected in a wet rotating denuder, while particles are grown to droplets containing the water soluble inorganic ions at high supersaturation in the steam jet aerosol collector. The liquid samples are then analysed online via an ion chromatography system [18].

SI.6.4 Particle and droplet properties and composition: Particulate composition was measured with Aerosol Mass Spectrometry (AMS): a C-ToF-AMS was used for the cloud droplet residual fraction and an HR-ToF-AMS for the interstitial particle fraction at Schmücke (Aerodyne Research, Inc.). Cloud droplet residual particle composition was also measured with the single particle laser ablation aerosol mass spectrometer ALABAMA (Aircraft-based Laser Ablation Aerosol MAss spectrometer) at the CVI inlet at Schmücke. Cloud droplet size distributions were measured with an FSSP-100 (Forward Scattering Spectrometer Probe, PMS Inc.) at Schmücke, and cloud droplet residual and interstitial particle size distributions were measured with an optical particle counter (OPC; Grimm model 1.109) and a scanning mobility particle sizer (SMPS).

S2.1. Calculation of α_{cloud}

The changes in SO₂ isotopic composition during passage through the cloud in the three measurement periods are shown in Table S3. The fractionation factor α_{cloud} for SO₂ removal as the air parcel passes through the cloud can be compared to fractionation factors for known reactions to determine the major in-cloud removal pathway. The calculations are described in the following paragraphs, with FCE 7.1 used as an example to illustrate the calculations. α_{cloud} is calculated from the Rayleigh equations [19, 20]:

$$\alpha_{\text{cloud}} = \frac{\ln\left(\frac{R_{\text{downwind}}}{R_{\text{upwind}}}\right)}{\ln(f)} + 1 \quad (1)$$

where R_{upwind} and R_{downwind} are the isotope ratios $^{34}\text{S}/^{32}\text{S}$ of SO₂ at the upwind and downwind sites, which represent the initial and residual SO₂ isotopic composition respectively, and f is the fraction of the upwind SO₂ remaining at the downwind site. The values of R_{upwind} and R_{downwind} are 0.045470 ± 0.000083 and 0.043818 ± 0.000056 respectively for FCE 7.1 and the raw value of f for FCE 7.1 is 0.42, as shown in Table S2 (one minute-SO₂ concentrations are shown in Figure S1). Using Equation 1, we calculate an α_{cloud} of $43 \pm 11\%$. Corrections to f due to SO₂ added between the upwind and downwind stations are described below.

Dry deposition could introduce isotopic fractionation, as it is limited by the diffusion rate [21]. We estimate the value of α_{drydep} as the ratio of $D_{\text{air}}(^{34}\text{SO}_2)$ to $D_{\text{air}}(^{32}\text{SO}_2)$: $\alpha_{\text{drydep}} = 0.991$, where D_{air} is the diffusion coefficient of the molecule in air. However, the estimated dry deposition flux of SO₂ is $\sim 0.5 \text{ day}^{-1}$ [22], so dry deposition is expected to remove $< 1\%$ of SO₂ in the short time period (~ 25 minutes) between upwind and downwind measurements, causing the downwind (residual) SO₂ to be just 0.09% enriched in ^{34}S compared to the upwind SO₂. Dry deposition is therefore not corrected for when calculating α_{cloud} .

SO₂ sources between the upwind and downwind stations also affect the calculation of α_{cloud} , by altering both the calculated value of f and the $\delta^{34}\text{S}$ of downwind SO₂: Additional ‘concent-

tration' means the actual fraction reacted ($1 - f$) is higher than assumed by simply looking at the decrease in SO_2 concentration between the upwind and downwind stations, while the $\delta^{34}\text{S}$ value of the added SO_2 directly alters the measured SO_2 isotopic composition. These two parts were treated separately to better consider the uncertainty.

Changes in SO_2 concentration during designated 'non-cloud events' were used to estimate possible SO_2 sources between the stations. Cross-correlation of ozone and other species was used to select non-cloud events with good connected flow conditions. During day-time non-cloud events, the direction of the SO_2 concentration change between the upwind and downwind stations varied due to the strong dependence of oxidant concentrations (OH and H_2O_2) on the level of solar radiation. At night SO_2 clearly increased (by $10.1 \pm 0.2 \text{ nmol m}^{-3}$) between the upwind and downwind stations in non-cloud events due to local inputs and the absence of photochemically-generated oxidants. As HO_2 and OH radical concentrations are very low during cloud events, it is likely that there is a net addition of SO_2 for which the best estimate is the average addition seen between upwind and downwind sites during the night-time non-cloud events. The impact of additional 'concentration' on α_{cloud} was determined by estimating a corrected f value:

$$f_{\text{corrected}} = \frac{[\text{SO}_2]_{\text{downwind}}}{[\text{SO}_2]_{\text{upwind}} + [\text{SO}_2]_{\text{added}}} \quad (2)$$

where $[\text{SO}_2]_{\text{added}}$ is $10.1 \pm 0.2 \text{ nmol m}^{-3}$, as determined from the non-cloud events. This correction results in a f value of 0.11 ± 0.14 for FCE 7.1 (as shown in Table S2), and an α_{cloud} of $16.7 \pm 9.4\%$.

The concentration of SO_2 increased between the upwind and downwind stations during the one cloud-free period when sulfur isotope measurements were taken (NC 1, see Table S2), and comparison of upwind and downwind $\delta^{34}\text{S}$ values showed the $\delta^{34}\text{S}$ of the added SO_2 was $7.4 \pm 3.4\%$ according to:

$$[\text{SO}_2]_{\text{added}} \cdot R_{\text{added}} = [\text{SO}_2]_{\text{downwind}} \cdot R_{\text{downwind}} - [\text{SO}_2]_{\text{upwind}} \cdot R_{\text{upwind}} \quad (3)$$

Upwind and downwind concentrations and isotopic compositions are given in Tables S2 and S3, and the concentration of SO₂ added is found from ([SO₂]_{downwind} - [SO₂]_{upwind}). This estimate of R_{added} assumes no significant fractionation due to removal of SO₂ between the stations. SO₂ addition can most likely be attributed primarily to mixing of free tropospheric SO₂, as there are no major SO₂ sources between the stations. Free tropospheric SO₂ is long-lived and well-mixed compared to boundary layer SO₂, so it can be assumed that the free tropospheric SO₂ concentration and $\delta^{34}\text{S}$ is similar across all measurement periods [23, 24]. The effect of adding SO₂ on isotopic composition was determined by calculating a corrected value for the upwind SO₂ isotopic composition according to:

$$R_{\text{upwind,corrected}} = \frac{[\text{SO}_2]_{\text{upwind}} \cdot R_{\text{upwind}} + [\text{SO}_2]_{\text{added}} \cdot R_{\text{added}}}{[\text{SO}_2]_{\text{upwind}} + [\text{SO}_2]_{\text{added}}} \quad (4)$$

$R_{\text{upwind,corrected}}$ for FCE 7.1 is 0.044961 ± 0.00097 (as shown in Table S2), resulting in an α_{cloud} of $29.7 \pm 9.9\text{‰}$ using the raw value of f . Using both corrected f and corrected R_{upwind} , the value of α_{cloud} is $11.6 \pm 9.9\text{‰}$ for FCE 7.1, as reported in Table 1.

Accounting for the effect of SO₂ addition on f reduces the magnitude of the calculated α_{cloud} by an average of 10.5‰ for the three events, while accounting for the effect of SO₂ addition on $\delta^{34}\text{S}$ increases the calculated α_{cloud} by an average of only 3.6‰ for the three events. The values of α_{cloud} reported in Table 1 of the main article are corrected for the effect of SO₂ addition on both f and $\delta^{34}\text{S}$. Although the correction carries some uncertainties due to entrainment during cloud periods, it improves the overall accuracy of the calculated α_{cloud} . The correction, however, changes only the magnitude of α_{cloud} and not the direction of isotopic fractionation, therefore the inferred dominant oxidation pathways shown in Table 1 are unaffected by the correction and its uncertainties.

α_{cloud} will not be representative of a single process but will be the sum of all the SO₂ removal processes occurring in the cloud:

$$\alpha_{\text{cloud}} = \frac{f_1 \cdot \alpha_1 + f_2 \cdot \alpha_2 \dots f_n \cdot \alpha_n}{f_1 + f_2 \dots f_n} \quad (5)$$

when n different SO₂ removal processes are acting in the cloud, assuming processes are occurring simultaneously and at constant relative rates. This is a valid assumption as the relative decrease in [SO₂] between upwind and in-cloud stations was equal to the decrease between in-cloud and downwind stations, showing that the pseudo-first order rate of SO₂ oxidation was approximately constant throughout the cloud.

S2.2. Using NanoSIMS S-isotope results to resolve sulfate addition to different particle classes

The particle-specific change in sulfur isotopic composition after passage through the cloud shows which sulfate sources dominate for the different particle classes. Only two particle types - 'mixed particles' (Fig. 1 A and B; containing a mixture of secondary organic aerosol (SOA) and secondary inorganic aerosol (SIA)) and mineral dust (Fig. 1 E and F) - consistently showed a significant increase in sulfur signal both in the SEM and NanoSIMS analysis between the downwind and upwind sample. Thus, it was concluded only these particle types gained a significant amount of sulfate from in-cloud processing. Other particle types such as soot (Fig. 1 C) and coated soot (Fig. 1 D) may have gained a small amount of sulfate, but the quantity of sulfur found in such particles was typically too small for isotope analysis. Given the lower number concentration of soot compared to mixed particles, the low fraction of soot particles <600 nm that activated and the insignificant amount of sulfate added to this particle class, soot and coated soot particles do not seem to gain any significant quantity of sulfur through the in-cloud sulfur cycle.

The $\delta^{34}\text{S}$ of sulfate that would be added from the different sources is shown in Table S4. The values concerning SO_2 oxidation are calculated from the upwind isotopic composition of SO_2 , the fraction of SO_2 lost in the cloud, and the fractionation factors shown in Tables 1 and S4. The isotopic composition of sulfate added from condensing H_2SO_4 and freshly nucleated particles was found from the upwind and downwind H_2SO_4 isotopic compositions, shown in Table S3. The observed changes in the $\delta^{34}\text{S}$ of different particle types between the upwind and downwind stations, shown in Table S5 (a complete list of all particles measured can be found in Table S6), were compared to the values in Table S4 to determine the dominant sulfate source for each particle type. The direction of change, rather than the absolute isotopic composition of downwind sulfate, allowed the dominant sulfate source to be identified. Mixed particle results are not size-resolved while mineral dust results are, as all mixed particles were smaller than $\sim 1 \mu\text{m}$ (see S1.3). However, a general trend was seen whereby smaller particles showed higher $\delta^{34}\text{S}$ values, suggesting more heavy sulfate was added to smaller than larger particles from condensation of H_2SO_4 (α_{cond}).

Sulfate added from the TMI-catalysis pathway is isotopically distinct, as oxidation by this pathway favours the light isotope. Coarse mineral dust particles were the only particle class that became isotopically lighter between the upwind and downwind measurement stations, which shows that sulfate from TMI-catalysed oxidation was only added in significant quantities to this particle class. Slight changes in pH between upwind and downwind stations may cause a small amount of mineral dust-bound sulfate to be dissolved. However, this will not affect results, as the NanoSIMS employs a harsh ionisation technique which sputters all sulfur present in the dust. It will therefore 'see' the mineral dust-bound sulfate equally whether it was dissolved in cloud water or not. Moreover, if significant sulfur had been present in the dust core, the ^{32}S signal would have remained stable or increased with depth in the unprocessed dust (upwind dust). This was not the case; rather, sulfur was found to be enriched at the surface.

S2.3. Analysis of particle identity and chemical composition with SEM and NanoSIMS

Scanning electron microscope (SEM) measurements were used to classify different particle types and investigate their chemical composition. The particulate samples could be directly analysed in the SEM after collection without any further treatment. A LEO 1530 field emission SEM with an Oxford Instruments ultra-thin-window energy-dispersive x-ray detector (EDX) was run in automatic mode, taking regularly-spaced images of the coarse and fine filters at 6500 \times and 19500 \times magnification respectively. The SEM was operated with an accelerating voltage of 15 keV, a 60 μm aperture and a working distance of 9.6 mm. “High current mode” was used to increase the EDX signal and improve elemental sensitivity. The SEM automatic analysis leaves a grid pattern on the gold-coated filters that is visible in the CCD camera of the NanoSIMS, which allows NanoSIMS and SEM images of the filters to be matched. Matching of SEM and NanoSIMS analyses means that different particle types can be identified in the NanoSIMS, so that isotopic compositions could be resolved for different particle classes.

The particle size distributions for different particle types, summarised in Table S7, were measured with the SEM as described in [25]. Scanning electron microscopy determines the volume equivalent diameter, which was converted to aerodynamic equivalent diameter using an average particle density of 1.5 g cm⁻³ according to the methodology described in [26]. The morphology and EDX spectrum of the particles were used to determine the particle type, examples of which are shown in Figure 1 of the main article. The ALABAMA results (Aircraft-based Laser Ablation Aerosol MAss spectrometer, S1.6) are shown in Table S7 for comparison. Comparisons are only relative, particularly for dust, as the definition of mineral dust from SEM morphological/EDX analysis is narrower than the range of spectra which are identified as dust in the ALABAMA. Particularly in the smaller size fraction (150-600 nm), many particles which are identified as dust by the ALABAMA are classified as salts or secondary inorganic aerosol in the SEM.

S2.4. Explaining the different oxidation regimes

Physical and chemical parameters measured during the cloud events were investigated to explain the different oxidation regimes in FCE 11.2 and 11.3 compared to FCE 7.1. FCE 11.2 and 11.3 had a higher liquid water content (0.14 g m^{-3} for FCE 7.1 compared to 0.37 and 0.32 g m^{-3} for FCE 11.2 and 11.3 respectively), while temperature, wind direction, particle number concentration and other meteorological and physical parameters were similar. Chemical parameters showing some variation between the three events are presented in Figure S2.

Organic compounds such as oxalate can complex with TMIs, reducing their efficiency as catalysts for SO_2 oxidation [27]. The bulk organic concentration agrees within the variability for all three events (2.7 ± 2.1 , 3.2 ± 1.6 and $4.4 \pm 2.4 \mu\text{g m}^{-3}$ for FCE 7.1, 11.2 and 11.3 respectively), and the air parcels passed over the same area of forest directly preceding the events, so there is no evidence that this affected the sulfur cycle at HCCT-2010. The only chemical parameter which is significantly different for FCE 7.1 compared to FCE 11.2 and 11.3 is upwind NH_3 (1.15 ± 0.07 , 0.56 ± 0.13 and $0.76 \pm 0.08 \mu\text{g m}^{-3}$ for FCE 7.1, 11.2 and 11.3 respectively). An increase in ammonia could buffer cloud droplets, allowing more oxidation by O_3 , however cloud water pH (both bulk as shown in Figure S2 and size-resolved from 3- and 5-stage impactor measurements) was too low (<5) for significant oxidation by O_3 in all events [28]. The observed steady state removal rate of SO_2 is also inconsistent with oxidation by O_3 , which is a strongly self-limiting reaction [29].

The TMI concentrations measured in cloud water during the three events, shown in Figure S3, can provide further insight into the different oxidation regimes. There are some noticeable differences in the cloud water TMI concentrations between the three events which suggest that the TMIs have a different source in FCE 7.1 compared to FCE 11.2 and 11.3. For example, the Ni^{2+} concentration is twice as high as the Cu^{2+} concentration in FCE 7.1, whereas during FCE

11.2 and 11.3 the Ni^{2+} and Cu^{2+} concentrations are roughly equal. The Fe^{3+} concentration is lower during FCE 7.1 than the other two events. From these and other differences we can infer that the source of TMIs was different during FCE 7.1 than during FCE 11.2 and 11.3. It is therefore likely that concentrations of TMIs such as Ti and Cr, which can be leached in significant amounts from mineral dust [12] and even at very low concentrations increase the rate of oxidation in mixtures so that it is much greater than the sum of the individual rates [30, 31, 12], were also significantly different between FCE 7.1 and FCE 11.2 and 11.3. Only the total concentrations of these metals (measured as described in S1.5 and shown in Table S8), and not the soluble concentrations or speciation, were measured during HCCT. The large discrepancy between upwind and downwind concentrations during FCE 7.1 means that the absolute total TM concentrations in the cloud are uncertain, and only relative amounts of different TMs should be interpreted. The total concentrations give a guide as to what could be leached from dust, however speciation, aging, and many other factors mean that the total concentration is not representative of the aqueous concentration. Moreover, studies have shown that catalysis by undissolved TMs on the dust surface is insignificant compared to catalysis by leached TMIs [32, 31], thus the total metal concentrations may not relate to the SO_2 oxidation catalysis rate.

In summary, during FCE 11.2 and 11.3, natural TMIs derived from mineral dust provided a TMI mixture that could strongly oxidise SO_2 , while during FCE 7.1 coarse mineral dust was not the major TMI source and the TMIs present did not cause rapid SO_2 oxidation. There are two possible explanations: Dust was not present during FCE 7.1, or dust does not activate during FCE 7.1. Particle size distributions from the OPC confirm that the dust mode was present in the aerosol population in FCE 7.1, but remained in the interstitial phase (Figure S4A), while activated fractions from SMPS data confirm that overall activation was lower during FCE 7.1 than during FCE 11.2 and 11.3, particularly at larger particle sizes (Figure S4B). Supersaturation cannot be measured, thus LWC will be used as the best available proxy. The LWC is more

than twice as high in FCE 11.2 and 11.3 than in FCE 7.1, so although LWC is not a perfect proxy for supersaturation, the similar meteorological conditions during the three events mean that LWC will give an adequate reference for supersaturation. The LWC, and therefore most likely the supersaturation, in FCE 7.1 was much lower than in FCE 11.2 and 11.3 (Table S2), and as mineral dust is relatively non-hygroscopic and a poor CCN, it was unable to activate during FCE 7.1 [33].

The activation hypothesis is supported by other aspects of the SEM and NanoSIMS results. Dust particles were found on the coarse interstitial filters, confirming that even particles up to 4-5 μm in diameter were not activated to droplets at the time of collection. Although these particles may have been ‘wet’ at the time of collection, the isotopic analyses showed no significant chemical changes occurred in these interstitial particles: The $\delta^{34}\text{S}$ values were not significantly different between the upwind and interstitial filters for any event, or any particle size or type. Thus, it is clear some large mineral dust particles were able to pass through the clouds in FCE 7.1 without activation to droplets $>5 \mu\text{m}$, and that this activation is necessary for significant sulfate production. This is in agreement with previous observations which showed that the scavenging efficiency of aerosol sulfate increases with liquid water content until $\sim 0.3 \text{ g m}^{-3}$ and that an LWC of 0.14 g m^{-3} is insufficient to activate many particles that will be CCN at $\text{LWC} > 0.3 \text{ g m}^{-3}$ [34], and with SEM observations from HCCT showing that fine mineral dust during FCE 11.2 was present only on the interstitial filter and therefore not activated. The ALABAMA observations also clearly show that both dust and soot activation was much lower in FCE 7.1 than FCE 11.2 and 11.3 (Table S7) supporting the hypothesis that mineral dust was activated in FCE 11.2 and 11.3 but not in FCE 7.1; no activated mineral dust was measured by ALABAMA in FCE 7.1.

S2.5. Calculating the rate of SO₂ oxidation via different pathways in the cloud

Chemical estimation calculations were performed to compare the theoretical contributions of the different pathways, based on published rate coefficients, with the isotopic results measured during the HCCT campaign. The percentage of sulfate production attributed to each pathway is shown in Figure S5. Cloud water concentrations of S(IV), H₂O₂ and transition metals were measured directly during HCCT as described in S1.5 and S1.6, while the aqueous ozone concentration was calculated from the gas-phase measurements using Henry's Law. Where the concentration of Mn²⁺ was below the detection limit, it was set as 10% of the soluble iron concentration. The rates of S(IV) oxidation by H₂O₂ and O₃ are well-known and calculations were made according to the kinetic data considered in the CAPRAM 3.0 mechanism [35]. The rate of oxidation catalysed by transition metal ions is not well constrained due to the rate-enhancing interactions between multiple transition metal ions in solution. Figure S5A shows the partitioning between oxidation pathways only accounting for synergistic interactions between Fe³⁺ and Mn²⁺ in solution, as measured by [36].

As outlined by [37], synergistic effects in transition metal catalysed reactions probably play an important role. However, it has been widely reported that synergistic effects can be positive and negative depending on many issues such as the interacting TMIs and their concentrations, and the pH and ionic strength of the solution. Investigations by [38] have shown the highest positive synergistic effect on the S(IV) oxidation for Fe³⁺ and Mn²⁺ beside other investigated TMIs. The results in Figure S5B show partitioning when it is assumed that all other transition metals in solution - instead of Mn²⁺ only - also contribute to synergistic rate enhancement. This rough estimation has been made because interactions between metal ions other than Fe³⁺ and Mn²⁺ have not been examined in kinetic studies. Due to the fact that the synergistic effect for Fe³⁺ and Mn²⁺ is strong, the calculation shown in Figure S5B represents only an upper-limit estimate of possible interactions and should be used with great care.

The results in Figure S5A show that TMI-catalysed oxidation is strongly underestimated when only Fe³⁺-Mn²⁺ interactions are considered; while the isotopic results showed that TMI-catalysis dominated oxidation for FCE 11.2 and 11.3, the model calculated that just 3 and 1% of sulfate respectively is produced by this pathway. When all TMIs present in cloud water are considered (Figure S5B), a much greater proportion of oxidation is modelled to occur via the TMI-catalysis pathway. However, in this case TMI-catalysis is also expected to dominate in FCE 7.1, which was not seen in the isotopic results. This shows that not all TMIs are equally active catalytically and the particular mixture of TMIs is important for catalytic activity. Kinetic laboratory studies considering interactions between the many TMIs present in cloud water are needed before models can accurately assess the extent and importance of this oxidation pathway.

S2.6. Calculation of the reactive uptake coefficient

The reactive uptake coefficient γ_{obs} for SO₂ uptake and oxidation by different pathways in the cloud can be estimated according to [39]:

$$\gamma_{\text{obs}} = \frac{4F_g}{\bar{c}A} \frac{\Delta n}{n} \quad (6)$$

where F_g is the carrier gas flow rate (cm² s⁻¹), \bar{c} is the mean thermal velocity (cm s⁻¹; $\sqrt{\frac{3k_B T}{m}}$), A is the total droplet surface area (cm²) and $\frac{\Delta n}{n}$ is the reduction in gas concentration. To adapt this equation to the observations during HCCT-2010, the cloud was conceptualised as a flow reactor: the wind speed was used as the flow rate, the droplet surface area for different droplets types was estimated from the number concentration and the mean droplet radius for the event, and the maximum possible value of γ_{obs} was calculated as if SO₂ oxidation was only occurring on the particle type of interest. The calculated uptake coefficients are shown in Table S9. The gas phase diffusion rates and accommodation coefficients for SO₂ in both oxidation reactions will be the same, thus the values show that at HCCT-2010 the rate of SO₂ oxidation by TMI-

catalysis in cloud droplets formed on coarse mineral dust was >1800 times faster than oxidation by H_2O_2 on mixed particles.

S2.7. Comparison of previous measurements of ambient sulfur isotopes ratios with known fractionation factors

Measurements of $\delta^{34}\text{S}$ from previous studies can provide an estimate of the importance of transition metal catalysed oxidation to compare with the rate of the reaction estimated in this study (Table S10). A number of studies have measured the $\delta^{34}\text{S}$ of SO_2 and sulfate simultaneously in the environment, and the average measured difference in $\delta^{34}\text{S}$ between SO_2 and product sulfate is $-0.3 \pm 2.2\text{‰}$ in rural environments [40, 41] and $4.6 \pm 2.5\text{‰}$ in urban environments [42, 43, 44]. No studies at coastal sites were considered in this analysis. [45] modelled the partitioning between SO_2 oxidation pathways for the pre-industrial period, and these values were used to calculate a baseline difference between $\delta^{34}\text{S}$ of SO_2 and sulfate to compare with measurements, as shown in Table S10. The relative rates of OH , H_2O_2 and O_3 oxidation were kept constant and the proportion of SO_2 oxidised by the TMI-catalysis pathway was increased to give a $\delta^{34}\text{S}$ value fitting the measurements.

This comparison shows that the model underestimates transition metal catalysed oxidation by 1% in urban and 58% in rural environments, and suggests the pathway is significantly more important in rural than in urban environments. The results suggest globally the pathway is underestimated by 35%. This is consistent with the large underestimation in modelled rates of transition metal-catalysed oxidation compared to the rate seen during the rural measurements at HCCT. The underestimation may be less important in the urban environment because mineral dust contributes a smaller proportion of the total transition metal ions [46] and concentrations of O_3 and H_2O_2 are much higher. The estimate does not account for changes in partitioning between the OH , O_3 and H_2O_2 oxidation pathways that may occur as a result of increased

oxidation by the TMI pathway. It is likely the aqueous pathways H_2O_2 and O_3 would decrease more than the OH pathway, which would increase the proportion of oxidation attributed to the TMI pathway as the fractionation factors for oxidation by H_2O_2 and O_3 are higher than the fractionation factor for oxidation by OH [4]; thus 35% is a conservative estimate of how strongly the pathway is globally underestimated. The comparison can only provide an estimate of the importance of the various pathways as the measurements are not seasonally and globally representative; the results are most relevant to the USA and Europe where the majority of the measurements were made.

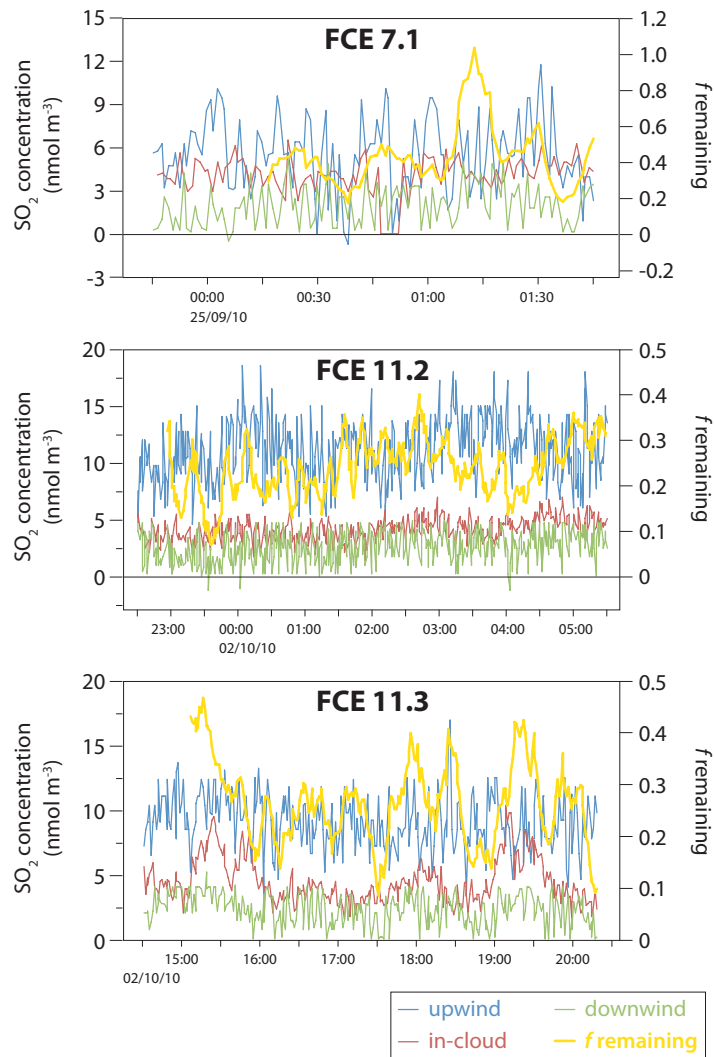


Figure S1. Upwind, in-cloud and downwind SO₂ concentrations (blue, red and green respectively) during HCCT-2010. Measurements are described in S1.6. *f* remaining (yellow) is the fraction of SO₂ remaining after the cloud, calculated by dividing the one-minute concentrations measured downwind by the concentrations measured upwind, with a 25 minute lag-time to account for transport. The lag-time was determined from SF₆ experiments used to monitor connected flow as described in S1.2.

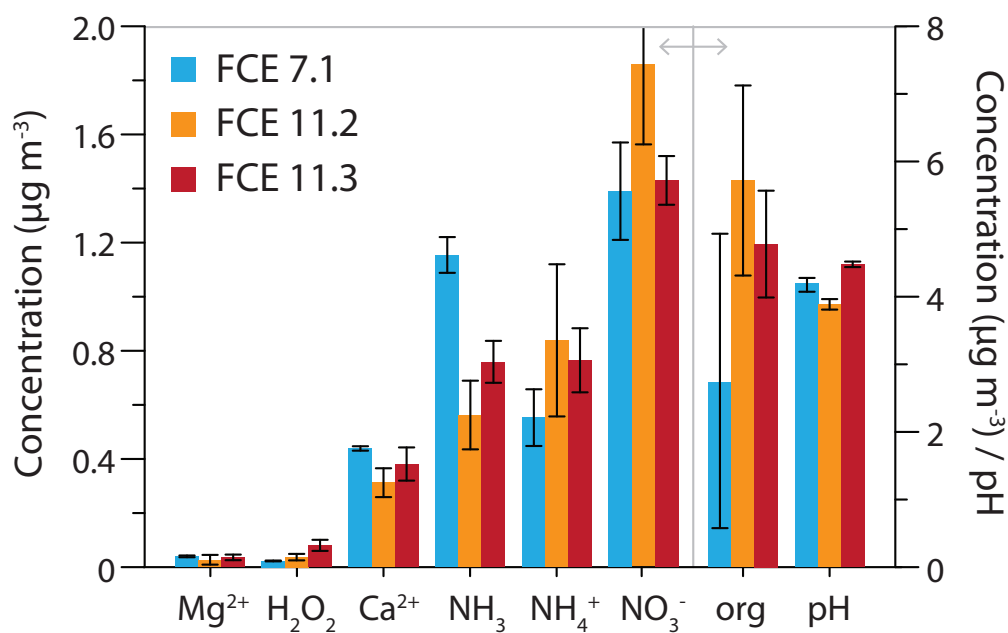


Figure S2. Concentrations of various compounds measured during HCCT-2010. Mg²⁺, Ca²⁺, NH₃, NH₄ and NO₃⁻ were measured at the upwind station with MARGA, H₂O₂ was measured in cloud water, 'org' is the organic matter concentration in cloud droplet residuals measured by AMS and pH is the bulk cloud water pH.

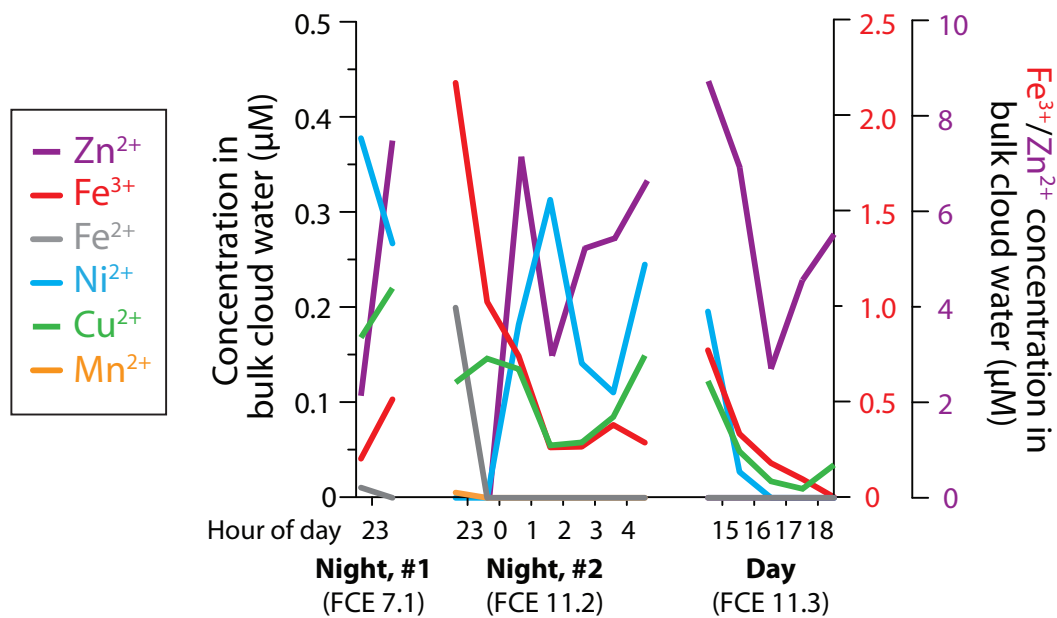
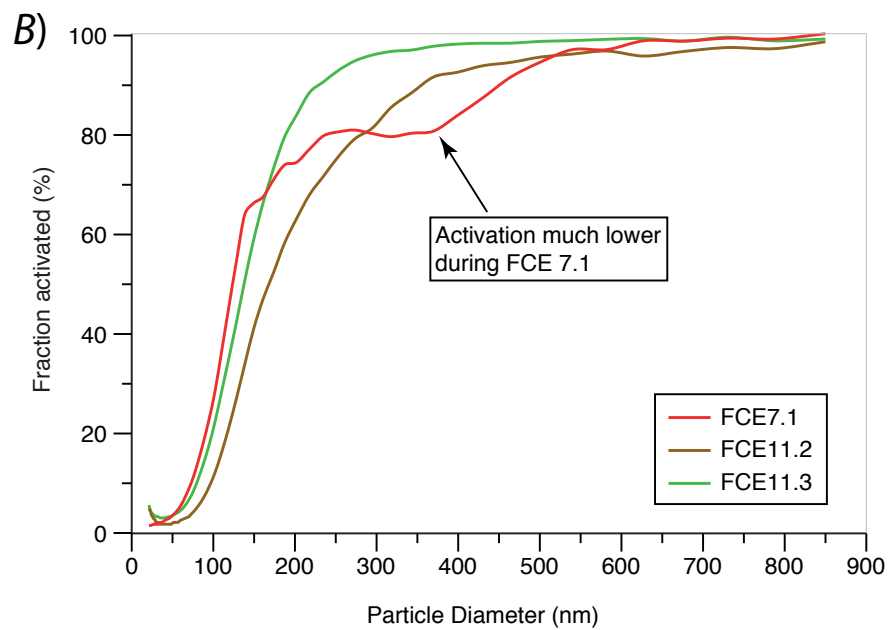
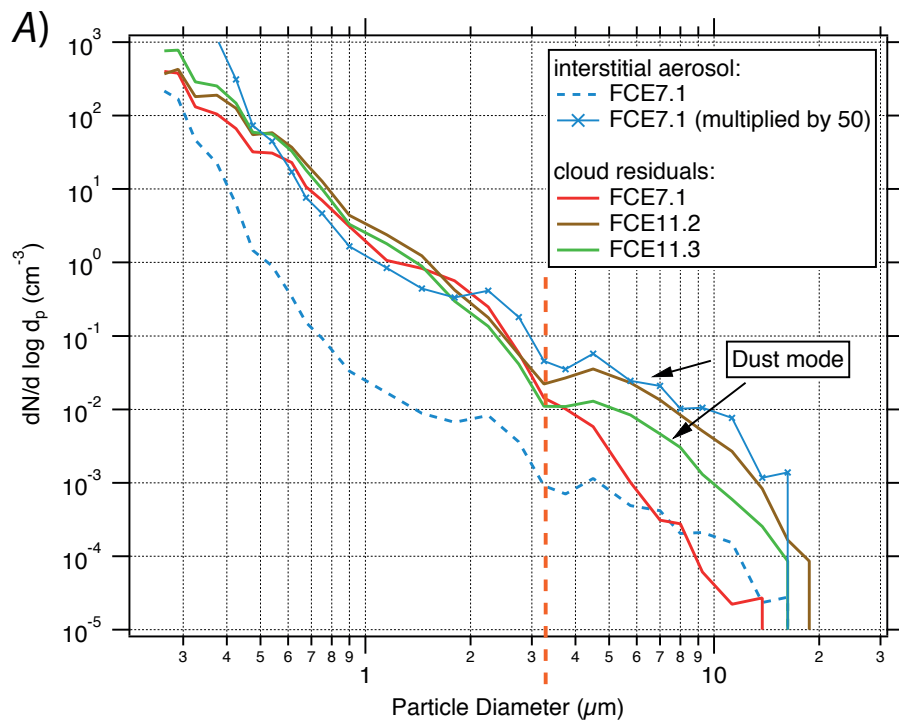


Figure S3. Concentrations of TMIs in cloud water during HCCT-2010; Fe³⁺ and Zn²⁺ are shown on the right-hand axes and all other ions on the left-hand axis.

Figure S4 (following page). A) Particle size distribution from the HCCT-2010 campaign OPC measurements showing the dust mode (particles larger than indicated by the dashed orange line) is found in the cloud residuals during cloud events FCE 11.2 and 11.3. In contrast, during FCE 7.1 the dust particles are found in the interstitial aerosol (blue line, scaled by factor 50 for comparison), but not in the cloud residuals, showing that no large dust particles were activated during FCE 7.1. B) Fraction of particles activated as a function of particle size. 'Fraction activated' is the cloud droplet residual number concentration divided by the total (residual + interstitial) number concentration for a particular size bin, measured at the in-cloud measurement station with SMPS.



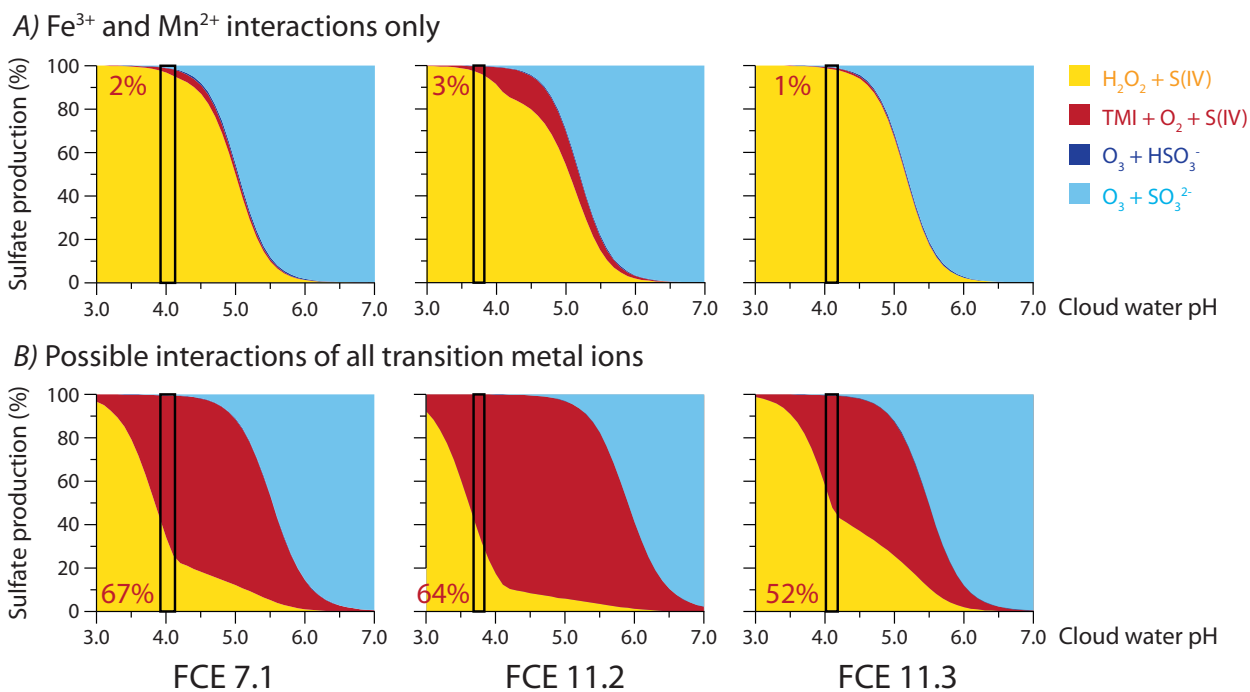


Figure S5. Calculations showing the proportion of sulfate production accounted for by different oxidation pathways with pH for three cloud events during HCCT-2010. Oxidation by H_2O_2 is shown in yellow, oxidation by O_2 catalysed by transition metal ions in red, and oxidation of HSO_3^- and SO_3^{2-} by O_3 in dark and light blue respectively. The pH range measured in cloud droplets on the three stages of the cloud water impactor is marked with a black outline, where the left-hand side (most acidic) represents the smallest droplets. The percentage of sulfate produced by the catalytic pathway at the median pH is shown in red text. A) Only interactions between Fe^{3+} and Mn^{2+} are considered, as measured by [36]. B) The interactions are calculated considering the interactions between Fe^{3+} and the total soluble non-iron transition metal ion concentration based on kinetic data for the Fe^{3+} - Mn^{2+} synergism from [36].

Model	References	AR4	AeroCom	Sulfur Species	Oxidation Pathways			% in-cloud
					O ₃	TM-cat	Other	
OsloCTM2	[47]	✓	✓	SO ₂ , SO ₄ , DMS, MSA, H ₂ S	✓	✓	HO ₂ NO ₂	83 (43)
SUNYA/UiO GCCM	[48, 49]	✓		SO ₂ , SO ₄ , DMS, MSA	✓		HO ₂ NO ₂	76
ECHAM5-HAMMOZ	[50, 51]	✓		SO ₂ , SO ₄ , DMS, MSA	✓		het. ox. ¹	
GEOS-Chem v822	[52]	✓	✓	SO ₂ , SO ₄ , DMS, MSA	✓			
MIROC-ESM	[53]	✓		SO ₂ , SO ₄ , DMS, COS	✓			
CSIRO Mk2 GCM	[54]	✓		SO ₂ , SO ₄ , DMS	✓			82 (47)
NCAR CCM3	[55, 56]	✓		SO ₂ , SO ₄ , DMS	✓			82 (56)
GLOMAP	[57, 58]		✓	SO ₂ , SO ₄ , DMS, MSA, DMSO, CS ₂ , COS				70 (35)
GISS ModelE/TOMAS ²	[59, 60, 61]	✓	✓	SO ₂ , SO ₄ , DMS, MSA				75 (40)
GOCART	[22, 62]		✓	SO ₂ , SO ₄ , DMS, MSA				64 (27)
U.K. HiGEM ³	[63]	✓	✓	SO ₂ , SO ₄ , DMS				
IPSL-CM4	[64]	✓		No interactive atmospheric chemistry				

Table S1. Comparison of sulfur cycle representations in different global models. Models are listed in order of the complexity of their treatment of the sulfur cycle. ‘AR4’ indicates whether the model was used in the IPCC’s 4th climate assessment report, and ‘AeroCom’ indicates whether the model participated in the recent AeroCom intercomparison exercise, a global initiative to compare state-of-the-art aerosol modelling results with observations [65]. Oxidation pathways show the SO₂ oxidation pathways calculated in the model; all models except IPSL-CM4 include oxidation by ·OH radicals in the gas phase and H₂O₂ in the aqueous phase. ‘% in-cloud’ shows the amount of oxidation (and of total SO₂ removal) accounted for by in-cloud oxidation pathways. ¹Includes heterogeneous reactions on sea salt aerosol ($\gamma_{\text{SO}_2} = 0.05$ at $\text{RH} \geq 50\%$, $\gamma_{\text{SO}_2} = 0.005$ at $\text{RH} > 50\%$) and mineral dust ($\gamma_{\text{SO}_2} = 10^{-4}$). ²GISS GCM ModelE used in AR4 predictions, GISS-TOMAS participated in AeroCom; SO₂ oxidation chemistry unchanged. ³HiGEM is the new high resolution version of HadGEM; the sulfur cycle is the same in both models, and participation in AR4 and AeroCom refers to HadGEM.

	NC 1	FCE 7.1	FCE 11.2	FCE 11.3
Type	cloud-free	cloud	cloud	cloud
Date	29.09.10	24 - 25.09.10	01 - 02.10.10	02.10.10
Time (CEST)	08:30 - 16:00	23:45 - 01:45	22:30 - 05:30	14:30 - 20:00
LWC (g m ⁻³)	<0.1	0.14	0.37	0.32
T (°C)		8.3	6.2	7.7
[H₂O₂] (nmol m ⁻³)		0.9	1.1	2.4
[SO₂]_U (nmol m ⁻³)	5.8	7.1	12.0	9.8
[SO₂]_D (nmol m ⁻³)	16.2	3.4	4.7	5.0
<i>f</i>, raw		0.42	0.24	0.26
<i>f</i>, corrected		0.11	0.11	0.12

Table S2. Measurement periods for sulfur isotope analysis during the HCCT-2010 campaign. Local Time is Central European Summer Time (CEST). [SO₂]_U and [SO₂]_D (upwind and downwind SO₂ concentrations respectively), [H₂O₂], LWC and temperature (T; at Schmücke) represent average values for the measurement period. *f* (raw) is the fraction of SO₂ remaining after the cloud, calculated by dividing the one minute-concentrations measured downwind by the concentrations measured upwind, with a 25 minute lag-time to account for transport, and then averaging over the measurement period (one minute SO₂ concentrations are shown in Figure S1). The lag-time was determined from SF₆ experiments used to monitor connected flow as described in S1.2. *f* (corrected) is the fraction remaining with respect to oxidation once SO₂ addition between the stations has been accounted for, as described in S2.1.

		NC 1	FCE 7.1	FCE 11.2	FCE 11.3
SO₂	$\delta^{34}\text{S}$ upwind, raw (‰)	24.5 ± 0.9	29.6 ± 1.9	-9.4 ± 3.2	13.1 ± 1.4
	$\delta^{34}\text{S}$ upwind, corrected (‰)		18.1 ± 3.9	-3.6 ± 4.7	11.0 ± 3.7
	$\delta^{34}\text{S}$ downwind (‰)	19.3 ± 0.9	-7.8 ± 1.3	32.1 ± 1.2	34.1 ± 1.2
	Change in $\delta^{34}\text{S}$ (‰)	-11.0 ± 1.4	-37.4 ± 2.3	41.5 ± 3.4	21.0 ± 1.8
H₂SO₄	$\delta^{34}\text{S}$ upwind (‰)		36.8 ± 1.2	52.3 ± 2.8	44.1 ± 4.5
	$\delta^{34}\text{S}$ downwind (‰)		34.5 ± 3.7	47.8 ± 8.6	10.5 ± 3.8

Table S3. Isotopic composition of SO₂ and H₂SO₄ at the upwind and downwind measurement stations and the change in $\delta^{34}\text{S}$ of SO₂ from the upwind to the downwind station during the HCCT-2010 campaign. Values are shown with 1 σ error. ‘ $\delta^{34}\text{S}$ upwind, corrected’ is an estimate accounting for SO₂ added during passage through the cloud, as described in S2.1.

Source	α (‰)	FCE 7.1	FCE 11.2	FCE 11.3
SO ₂ ox, $\alpha_{\text{TMI-cat}}$	-9.5	22.4±1.9	-16.3±3.2	6.0±1.4
SO ₂ ox, α_{cloud}	See Table 1	56.8±7.2	-22.4±4.0	5.6±2.1
SO ₂ ox, $\alpha_{\text{H}_2\text{O}_2}$	15.1	40.9±1.9	1.5±3.2	24.2±1.4
SO ₂ ox, α_{surf}	9.6	39.0±1.3	-0.4±1.1	22.3±1.1
H ₂ SO ₄ , α_{cond}	n/a	37.3±5.0	54.8±5.6	44.8±4.5

Table S4. $\delta^{34}\text{S}$ values (‰) of the potential sources of sulfate that could be contributed to particles during their passage through an orographic cloud: the dominant SO₂ removal pathway in the cloud (α_{cloud}), SO₂ oxidation in the aqueous phase by TMI-catalysis (α_{TMIcat}) and by H₂O₂ ($\alpha_{\text{H}_2\text{O}_2}$) from [4], SO₂ oxidation on the surface of Sahara dust with no aqueous phase (ie. on interstitial particles; α_{surf}) from [12], and uptake/coagulation of sulfuric acid gas and freshly nucleated particles (α_{cond}).

	Particle Type	$\delta^{34}\text{S}_{\text{upwind}}$ (‰)	$\delta^{34}\text{S}_{\text{downwind}}$ (‰)	Change in $\delta^{34}\text{S}$
FCE11.2	Mixed particles	-2.5±19.1	19.8±5.5	22.3±19.9
	Fine mineral dust	10.6±6.9	14.1±7.5	3.5±10.7
	Coarse mineral dust	14.4±5.5	1.5±3.1	-12.9±6.3
FCE11.3	Mixed particles	7.3±3.5	15.9±2.5	8.6±4.3
	Fine mineral dust	10.7±3.4	27.3±6.2	16.6±7.1
	Coarse mineral dust	13.5±2.6	8.3±3.6	-5.2±4.4

Table S5. $\delta^{34}\text{S}$ values (‰, with 1 σ error) of particulate sulfate upwind and downwind of an orographic cloud during HCCT-2010. The source of sulfate added in the cloud can be determined by comparing the change in $\delta^{34}\text{S}$ with the $\delta^{34}\text{S}$ values for sulfate sources shown in Table S4. A complete list of all particles measured can be found in Table S6.

Table S6 (continued on following page). Complete list of particle measurements made by NanoSIMS on HCCT samples between February and May, 2011. Error is the combined counting statistical error and IMF error, as described in S1.4. UPW = upwind, CDR = cloud droplet residual (= in-cloud), INT = interstitial, DNW = downwind, Av. = weighted average. Where only one particle for a particular class is available, the error in the 'average' also accounts for the spot-to-spot error as measured on the standards.

	Particle Type	#	UPW (‰)	CDR (‰)	INT (‰)	DNW (‰)
FCE 11.2 (Night #2)	<i>Mixed particles</i>	1	14.9±4.2	31.5±3.9	9.4±5.4	6.8±4.6
		2	-14.7±3.3	40.7±17.0	20.4±9.0	13.7±4.2
		3	21.9±16.9	14.5±8.5	8.5±7.8	30.2±2.6
		4	18.3±9.0	17.9±5.6	10.5±6.1	23.2±4.2
		5	-7.5±12.0	22.9±8.5		52.2±11.1
		6	-17.3±9.4	11.4±5.2		39.1±11.0
		7		25.3±9.5		-24.2±15.5
		8		8.6±3.2		22.7±10.0
		9		1.5±3.6		-6.1±12.0
		10		8.5±3.2		15.2±4.9
		11		18.2±4.8		12.8±3.2
		12		8.1±4.5		
		13		18.4±3.5		
		14		5.1±2.8		
			Av.	-2.5±19.1	12.2±2.7	11.1±3.3
	<i>Fine mineral dust</i>	1	4.4±5.1		15.8±8.4	14.1±7.5
		2	20.5±6.6		6.4±7.0	
		3	11.3±8.9		6.1±9.6	
		4			7.6±7.9	
		Av.	10.6±6.9		8.9±4.0	14.1±9.5
	<i>Coarse mineral dust</i>	1	16.6±5.2	7.5±4.6	13.7±5.9	6.3±5.1
		2	-1.7±13.9	-1.8±8.5	11.8±4.0	-3.3±7.9
		3	6.4±5.2	12.0±10.7	13.2±7.5	-0.6±5.8
		4	13.4±5.2		10.3±8.2	-1.5±7.8
		5	27.4±6.2			
	Av.	14.4±5.5	6.2±3.8	12.2±2.8	1.5±3.1	

	Particle Type	#	UPW (‰)	CDR (‰)	INT (‰)	DNW (‰)
FCE 11.3 (Day)	<i>Mixed particles</i>	1	5.5±4.0	28.8±5.1	3.9±10.0	13.8±8.4
		2	1.2±5.7	13.0±4.1	6.4±19.6	2.6±8.8
		3	14.3±10.5	9.9±6.1	22.3±5.9	7.2±10.2
		4	-4.3±17.6	11.4±3.2	6.1±6.1	15.7±15.5
		5	29.0±10.3	11.8±5.0	8.7±5.7	2.6±12.2
		6	22.4±18.7	24.7±5.5	-12.2±12.9	22.9±5.1
		7	13.3±14.1	10.5±5.2	15.8±8.3	11.3±12.0
		8		12.2±4.6	18.6±13.5	15.4±10.5
		9		25.5±7.7	12.4±10.1	20.2±13.2
		10		7.8±5.3	15.8±4.9	17.9±4.2
		11		8.3±8.2	5.3±3.3	
		12		31.4±5.8		
		13		21.5±4.3		
		14		4.9±3.8		
	Av.	7.3±3.5	14.6±1.3	9.9±1.9	15.9±2.5	
	<i>Coated soot</i>	1	4.6±5.2	17.7±4.1		
		2		17.4±5.6		
		3		17.2±3.9		
		Av.	4.6±7.3	17.4±2.5		
	<i>Fine mineral dust</i>	1	9.7±4.3	34.7±4.4	9.2±3.7	27.3±4.2
		2	11.4±5.7		16.6±3.7	
		3	17.8±15.6		6.9±3.8	
		4			2.7±4.8	
		5			-6.7±3.8	
		6			-3.9±3.9	
	Av.	10.7±3.4	34.7±6.3	4.4±8.3	27.3±6.2	
	<i>Coarse mineral dust</i>	1	12.1±4.5	-2.3±3.8	8.5±12.5	10.7±6.8
		2	16.2±10.7	-3.9±7.6		10.7±6.9
		3	12.2±5.4	-3.4±7.4		11.4±21.6
		4	15.0±6.6			4.8±5.7
		5	14.9±5.2			7.7±20.4
	Av.	13.5±2.6	-2.8±3.1	8.5±14.6	8.3±3.6	

		<i>Cloud Droplet Residual</i>			<i>Interstitial</i>			Fraction activated (%)
		Number (cm^{-3})	Fraction (%)	N_a	Number (cm^{-3})	Fraction (%)	N_a	
FCE 7.1 nm	<i>ALABAMA - Soot</i>		10					
150-600 nm	<i>ALABAMA - Dust</i>		0					
FCE 7.1 nm	<i>ALABAMA - Soot</i>		4					
600-900 nm	<i>ALABAMA - Dust</i>		0					
FCE 11.2	Soot	14±9	20	23	125±13	64	72	10
150-600 nm	<i>ALABAMA - Soot</i>		18					
	Dust	0	0	0	0.002±0.003	0.001	1	0
	<i>ALABAMA - Dust</i>		5					
	PBA	1.3±0.9	2	3	0	0	0	100
	Mixed SOA/SIA	54±12	78	144	69±13	36	13	43
FCE 11.2	Soot	0.4±0.4	15	4	0	0	0	100
600-900 nm	<i>ALABAMA - Soot</i>		28					
	Dust	0.002±0.002	0.1	3	0.002±0.003	100	1	50
	<i>ALABAMA - Dust</i>		2					
	PBA	1.0±0.2	43	26	0	0	0	100
	Mixed SOA/SIA	1.0±0.5	42	30	0	0	0	100
FCE 11.2	Soot	0.2±0.1	16	6	0.1±0.1	80	1	66
>900 nm	Dust	0.009±0.004	0.7	18	0.02±0.01	17	10	31
	PBA	0.5±0.1	38	29	0.005±0.006	3	2	99
	Mixed SOA/SIA	0.7±0.2	49	109	0	0	0	100

		<i>Cloud Droplet Residual</i>			<i>Interstitial</i>			
		Number (cm^{-3})	Fraction (%)	N_a	Number (cm^{-3})	Fraction (%)	N_a	Fraction activated (%)
FCE 11.3	Soot	18 ± 5	14	13	28 ± 6	67	14	27
150-600 nm	<i>ALABAMA - Soot</i>		6					
	Dust	0.004 ± 0.009	0.003	2	0.004 ± 0.003	0.01	2	50
	<i>ALABAMA - Dust</i>		8					
	PBA	0	0	0	0	0	0	
	Mixed SOA/SIA	111 ± 9	86	132	14 ± 7	33	14	89
FCE 11.3	Soot	0.8 ± 0.3	29	5	0.1 ± 0.3	94	1	89
600-900 nm	<i>ALABAMA - Soot</i>		18					
	Dust	0.03 ± 0.02	1	10	0.006 ± 0.003	6	3	83
	<i>ALABAMA - Dust</i>		2					
	PBA	0.01 ± 0.01	0.3	2	0	0	0	100
	Mixed SOA/SIA	2.0 ± 0.6	70	17	0	0	0	100
FCE 11.3	Soot	0.1 ± 0.1	5	3	0	0	0	100
>900 nm	Dust	0.05 ± 0.02	3	24	0.032 ± 0.004	94	13	61
	PBA	0.03 ± 0.01	2	11	0.002 ± 0.004	6	1	94
	Mixed SOA/SIA	1.6 ± 0.2	90	53	0	0	0	100

Table S7 (previous two pages). Number concentrations of different particle types measured with SEM analysis from samples taken at the in-cloud station Schmücke during the HCCT-2010 campaign. Results from ALABAMA are shown in italics for comparison, and only ALABAMA results are available for FCE 7.1. 'N_a' is the number of particles counted in the SEM. 'Fraction' refers to the percentage of the total particle number concentration (within 'Droplet Residue' or 'Interstitial') that is represented by a particulate particle type. PBA = Primary Biological Aerosol. The 'Fraction activated' refers to the number of particles per cm³ of air found to belong to a certain type (e.g. PBA) and a certain size bin counted on the droplet residue filter, divided by the total number of particles per cm³ for the same type and same size bin at the in-cloud station (droplet residue + interstitial filter). The activation of a particle was therefore determined during SEM analysis by virtue of particles being found on the droplet residue filter, which indicates the particle was present in a droplet with >5μm aerodynamic diameter at the time of collection.

			Ti	V	Cr	Mn	Fe	Ni	Cu	Zn
Fine	FCE 7.1	U	0.68±0.27	0.02±0.13	7.05±0.42	0.49±0.09	22.22±0.36	0.17±0.04	0.01±0.05	6.02±0.32
		D	BDL	0.09±0.08	2.54±0.45	BDL	1.50±0.47	0.05±0.02	0.01±0.05	3.97±0.24
	FCE 11.2	U	0.17±0.07	0.02±0.03	0.37±0.26	0.07±0.01	1.97±0.56	0.26±0.03	0.11±0.02	1.21±0.22
		D	0.68±0.10	0.03±0.03	BDL	0.09±0.02	8.33±0.30	BDL	0.03±0.03	2.41±0.06
	FCE 11.3	U	0.07±0.12	BDL	0.30±0.19	BDL	0.73±0.24	0.01±0.01	0.05±0.04	2.90±0.12
		D	0.03±0.15	0.04±0.04	0.47±0.11	0.07±0.03	1.40±0.09	0.44±0.04	0.12±0.03	0.46±0.06
Coarse	FCE 7.1	U	1.93±0.38	0.12±0.05	12.78±1.20	1.83±0.46	86.59±3.09	2.25±0.17	0.36±0.08	3.00±0.30
		D	0.13±0.12	0.07±0.03	1.09±0.41	0.10±0.07	3.84±0.18	BDL	0.19±0.05	2.65±0.07
	FCE 11.2	U	0.19±0.09	0.04±0.02	0.50±0.11	0.24±0.07	4.24±0.52	0.23±0.03	0.08±0.02	1.29±0.06
		D	0.23±0.04	0.06±0.04	0.21±0.13	0.10±0.03	4.47±0.30	0.01±0.00	0.01±0.03	1.14±0.04
	FCE 11.3	U	0.18±0.10	0.03±0.01	BDL	0.04±0.02	6.57±0.40	BDL	0.07±0.05	2.06±0.08
		D	0.20±0.08	0.07±0.03	1.24±0.10	0.12±0.02	6.01±0.31	0.66±0.04	0.31±0.03	0.72±0.07

Table S8. Total transition metal concentrations (ng m^{-3}) measured with TXRF as described in S1.5. U = upwind, D = downwind. BDL = below detection limit. ‘Fine’ refers to the first two stages of the impactor collectors with a cut-off of $0.42 \mu\text{m}$, ‘coarse’ particles are $0.42 - 3.5 \mu\text{m}$ and are collected on the third and fourth impactor stages. There is a very large discrepancy between upwind and downwind concentrations during FCE 7.1 which may be due to the worse connected flow conditions, technical problems during upwind sampling, or uncertainty due to the short length of the event.

	Oxidant	FCE 11.2		FCE 11.3	
		γ_{obs}	% oxidised	γ_{obs}	% oxidised
Mineral dust	TMI catalysis	0.10 ± 0.03	92	0.03 ± 0.01	24
Mixed particles	H_2O_2	$5.7 \pm 1.5 \times 10^{-5}$	0.05	$1.4 \pm 0.4 \times 10^{-5}$	0.01
Ratio (TMI/ H_2O_2)		1800		1900	

Table S9. Reactive uptake coefficients for $\text{SO}_2 \rightarrow \text{SO}_4^{2-}$ in cloud droplets during HCCT-2010. ‘% oxidised’ refers to the proportion of SO_2 (g) taken up by the particle that goes on to be oxidised with an accommodation coefficient of $\alpha = 0.11$ [66]. It was not possible to calculate γ_{obs} for FCE 7.1 as equipment problems meant particulate was not collected.

	Sofen et al. (2011)	Urban	Rural
$f(\text{OH})$	0.27	0.27	0.08
$f(\text{H}_2\text{O}_2)$	0.5	0.5	0.15
$f(\text{O}_3)$	0.05	0.05	0.015
$f(\text{O}_2, \text{TMI-catalysed})$	0.18	0.18	0.76
$\delta^{34}\text{S}_{\text{SO}_4} - \delta^{34}\text{S}_{\text{SO}_2}, \text{ model } (\text{‰})$	4.7	4.6	-0.3
$\delta^{34}\text{S}_{\text{SO}_4} - \delta^{34}\text{S}_{\text{SO}_2}, \text{ measurements } (\text{‰})$		4.6 ± 2.5	-0.3 ± 2.2
Increase in TMI pathway	-	1%	58%

Table S10. Increase in transition metal catalysed oxidation of SO_2 from global baseline industrial-period model [45] required to account for measured differences in $\delta^{34}\text{S}$ of SO_2 gas and product sulfate in urban and rural environments.

References

1. M. O. Andreae, C. D. Jones, P. M. Cox, Strong present-day aerosol cooling implies a hot future. *Nature* **435**, 1187 (2005). [doi:10.1038/nature03671](https://doi.org/10.1038/nature03671)
2. M. Kulmala, U. Pirjola, J. M. Makela, *Nature* **404**, 66 (2000). [doi:10.1038/35003550](https://doi.org/10.1038/35003550)
3. S. Solomon *et al.*, in *Climate Change 2007: The Physical Science Basis. Contribution of Working Group I to the Fourth Assessment Report of the Intergovernmental Panel on Climate Change*, S. Solomon *et al.*, Eds. (Cambridge Univ. Press, New York, 2007), technical summary.
4. J. Langner, H. Rodhe, P. J. Crutzen, P. Zimmermann, Anthropogenic influence on the distribution of tropospheric sulphate aerosol. *Nature* **359**, 712 (1992). [doi:10.1038/359712a0](https://doi.org/10.1038/359712a0)
5. S. Mertes *et al.*, Evolution of particle concentration and size distribution observed upwind, inside and downwind hill cap clouds at connected flow conditions during FEBUKO. *Atmos. Environ.* **39**, 4233 (2005). [doi:10.1016/j.atmosenv.2005.02.009](https://doi.org/10.1016/j.atmosenv.2005.02.009)
6. D. Goto, T. Nakajima, T. Takemura, K. Sudo, A study of uncertainties in the sulfate distribution and its radiative forcing associated with sulfur chemistry in a global aerosol model. *Atmos. Chem. Phys.* **11**, 10889 (2011). [doi:10.5194/acp-11-10889-2011](https://doi.org/10.5194/acp-11-10889-2011)
7. K. N. Bower *et al.*, Observations and modelling of the processing of aerosol by a hill cap cloud. *Atmos. Environ.* **31**, 2527 (1997). [doi:10.1016/S1352-2310\(96\)00317-2](https://doi.org/10.1016/S1352-2310(96)00317-2)
8. C. F. Botha, J. Hahn, J. J. Pienaar, R. Vaneldik, Kinetics and mechanism of the oxidation of sulfur(IV) by ozone in aqueous solutions. *Atmos. Environ.* **28**, 3207 (1994). [doi:10.1016/1352-2310\(94\)00174-J](https://doi.org/10.1016/1352-2310(94)00174-J)
9. M. Chin *et al.*, A global three-dimensional model of tropospheric sulfate. *J. Geophys. Res.* **101**, 18667 (1996). [doi:10.1029/96JD01221](https://doi.org/10.1029/96JD01221)
10. G. P. Gervat *et al.*, Field evidence for the oxidation of SO₂ by H₂O₂ in cap clouds. *Nature* **333**, 241 (1988). [doi:10.1038/333241a0](https://doi.org/10.1038/333241a0)

11. D. A. Hegg, R. Majeed, P. F. Yuen, M. B. Baker, T. V. Larson, The impacts of SO₂ oxidation in cloud drops and in haze particles on aerosol light scattering and CCN activity. *Geophys. Res. Lett.* **23**, 2613 (1996). [doi:10.1029/96GL02419](https://doi.org/10.1029/96GL02419)
12. L. A. Barrie *et al.*, *Tellus* **53B**, 615 (2001).
13. L. Rotstajn, U. Lohmann, Simulation of the tropospheric sulfur cycle in a global model with a physically based cloud scheme. *J. Geophys. Res.* **107**, 4592 (2002).
[doi:10.1029/2002JD002128](https://doi.org/10.1029/2002JD002128)
14. T. Berglen, T. Berntsen, I. Isaksen, J. Sundet, A global model of the coupled sulfur/oxidant chemistry in the troposphere: The sulfur cycle. *J. Geophys. Res.* **109**, D19310 (2004).
[doi:10.1029/2003JD003948](https://doi.org/10.1029/2003JD003948)
15. D. A. Hegg, D. S. Covert, H. Jonsson, D. Khelif, C. A. Friehe, *Tellus* **56B**, 285 (2004).
16. A. L. Redington, R. G. Derwent, C. S. Witham, A. J. Manning, Sensitivity of modelled sulphate and nitrate aerosol to cloud, pH and ammonia emissions. *Atmos. Environ.* **43**, 3227 (2009). [doi:10.1016/j.atmosenv.2009.03.041](https://doi.org/10.1016/j.atmosenv.2009.03.041)
17. J. Tilly, M. Lewicki, Z. Tomaszewski, J. Toczowski, Use of ilmenite decomposition products in a gas desulphurisation process. *J. Chem. Technol. Biotechnol.* **52**, 301 (1991).
[doi:10.1002/jctb.280520303](https://doi.org/10.1002/jctb.280520303)
18. A. Rani, D. S. N. Prasad, P. V. S. Madnawat, K. S. Gupta, *Atmos. Environ.* **26A**, 667 (1992).
19. J. R. McCabe, J. Savarino, B. Alexander, S. L. Gong, M. H. Thiemens, Isotopic constraints on non-photochemical sulfate production in the Arctic winter. *Geophys. Res. Lett.* **33**, L05810 (2006). [doi:10.1029/2005GL025164](https://doi.org/10.1029/2005GL025164)
20. B. Alexander, R. J. Park, D. J. Jacob, S. L. Gong, Transition metal-catalyzed oxidation of atmospheric sulfur: Global implications for the sulfur budget. *J. Geophys. Res.* **114**, D02309 (2009). [doi:10.1029/2008JD010486](https://doi.org/10.1029/2008JD010486)
21. E. Harris *et al.*, Sulfur isotope fractionation during oxidation of sulfur dioxide: gas-phase oxidation by OH radicals and aqueous oxidation by H₂O₂, O₃ and iron catalysis. *Atmos. Chem. Phys.* **12**, 407 (2012). [doi:10.5194/acp-12-407-2012](https://doi.org/10.5194/acp-12-407-2012)

22. E. Harris *et al.*, Sulfur isotope fractionation during heterogeneous oxidation of SO₂ on mineral dust. *Atmos. Chem. Phys.* **12**, 4867 (2012). [doi:10.5194/acp-12-4867-2012](https://doi.org/10.5194/acp-12-4867-2012)
23. E. Harris, B. Sinha, P. Hoppe, S. Foley, S. Borrmann, Fractionation of sulfur isotopes during heterogeneous oxidation of SO₂ on sea salt aerosol: A new tool to investigate non-sea salt sulfate production in the marine boundary layer. *Atmos. Chem. Phys.* **12**, 4619 (2012). [doi:10.5194/acp-12-4619-2012](https://doi.org/10.5194/acp-12-4619-2012)
24. D. L. Sedlak *et al.*, The cloudwater chemistry of iron and copper at Great Dun Fell, U.K. *Atmos. Environ.* **31**, 2515 (1997). [doi:10.1016/S1352-2310\(96\)00080-5](https://doi.org/10.1016/S1352-2310(96)00080-5)
25. P. Laj *et al.*, Cloud processing of soluble gases. *Atmos. Environ.* **31**, 2589 (1997). [doi:10.1016/S1352-2310\(97\)00040-X](https://doi.org/10.1016/S1352-2310(97)00040-X)
26. P. Laj *et al.*, Experimental evidence for in-cloud production of aerosol sulphate. *Atmos. Environ.* **31**, 2503 (1997). [doi:10.1016/S1352-2310\(96\)00217-8](https://doi.org/10.1016/S1352-2310(96)00217-8)
27. K. Plessow, K. Acker, H. Heinrichs, D. Möller, Time study of trace elements and major ions during two cloud events at the Mt. Brocken. *Atmos. Environ.* **35**, 367 (2001). [doi:10.1016/S1352-2310\(00\)00134-5](https://doi.org/10.1016/S1352-2310(00)00134-5)
28. T. Ibusuki, K. Takeuchi, Sulfur dioxide oxidation by oxygen catalyzed by mixtures of manganese(II) and iron(III) in aqueous solutions at environmental reaction conditions. *Atmos. Environ.* **21**, 1555 (1987). [doi:10.1016/0004-6981\(87\)90317-9](https://doi.org/10.1016/0004-6981(87)90317-9)
29. T. E. Graedel, M. L. Mandich, C. J. Weschler, Kinetic model studies of atmospheric droplet chemistry: 2. Homogeneous transition metal chemistry in raindrops. *J. Geophys. Res.* **91**, 5205 (1986). [doi:10.1029/JD091iD04p05205](https://doi.org/10.1029/JD091iD04p05205)
30. I. Grgić, V. Hudnik, M. Bizjak, J. Levec, Aqueous S(IV) oxidation—I. Catalytic effects of some metal ions. *Atmos. Environ.* **25**, 1591 (1991). [doi:10.1016/0960-1686\(91\)90017-2](https://doi.org/10.1016/0960-1686(91)90017-2)
31. L. Pozzoli *et al.*, Trace gas and aerosol interactions in the fully coupled model of aerosol-chemistry-climate ECHAM5-HAMMOZ: 1. Model description and insights from the spring 2001 TRACE-P experiment. *J. Geophys. Res.* **113**, D07308 (2008). [doi:10.1029/2007JD009007](https://doi.org/10.1029/2007JD009007)

32. E. Sofen, B. Alexander, S. A. Kunasek, The impact of anthropogenic emissions on atmospheric sulfate production pathways, oxidants, and ice core $\Delta^{17}\text{O}(\text{SO}_4^{2-})$. *Atmos. Chem. Phys.* **11**, 3565 (2011). [doi:10.5194/acp-11-3565-2011](https://doi.org/10.5194/acp-11-3565-2011)
33. T. D. Jickells *et al.*, Global iron connections between desert dust, ocean biogeochemistry, and climate. *Science* **308**, 67 (2005). [doi:10.1126/science.1105959](https://doi.org/10.1126/science.1105959)
34. S. Solomon *et al.*, Eds., *Climate Change 2007: The Physical Science Basis. Contribution of Working Group I to the Fourth Assessment Report of the Intergovernmental Panel on Climate Change* (Cambridge Univ. Press, New York, 2007).
35. Centre on Emission Inventories and Projections for the European Monitoring and Evaluation Programme, www.ceip.at/webdab-emission-database/.
36. A. Tilgner, B. Heinold, A. Nowak, H. Herrmann, Meteorological characterisation of the FEBUKO hill cap cloud experiments, Part I: Synoptic characterisation of measurement periods. *Atmos. Environ.* **39**, 4185 (2005). [doi:10.1016/j.atmosenv.2005.02.006](https://doi.org/10.1016/j.atmosenv.2005.02.006)
37. B. Heinold *et al.*, Meteorological characterisation of the FEBUKO hill cap cloud experiments, Part II: Tracer experiments and flow characterisation with nested non-hydrostatic atmospheric models. *Atmos. Environ.* **39**, 4195 (2005). [doi:10.1016/j.atmosenv.2005.02.036](https://doi.org/10.1016/j.atmosenv.2005.02.036)
38. A. Schwarzenboeck, J. Heintzenberg, S. Mertes, Incorporation of aerosol particles between 25 and 850 nm into cloud elements: Measurements with a new complementary sampling system. *Atmos. Res.* **52**, 241 (2000). [doi:10.1016/S0169-8095\(99\)00034-4](https://doi.org/10.1016/S0169-8095(99)00034-4)
39. S. Mertes, K. Lehmann, A. Nowak, A. Massling, A. Wiedensohler, Link between aerosol hygroscopic growth and droplet activation observed for hill-capped clouds at connected flow conditions during FEBUKO. *Atmos. Environ.* **39**, 4247 (2005). [doi:10.1016/j.atmosenv.2005.02.010](https://doi.org/10.1016/j.atmosenv.2005.02.010)
40. P. Hoppe, NanoSIMS: A new tool in cosmochemistry. *Appl. Surf. Sci.* **252**, 7102 (2006). [doi:10.1016/j.apsusc.2006.02.129](https://doi.org/10.1016/j.apsusc.2006.02.129)
41. E. Gröner, P. Hoppe, Automated ion imaging with the NanoSIMS ion microprobe. *Appl. Surf. Sci.* **252**, 7148 (2006). [doi:10.1016/j.apsusc.2006.02.280](https://doi.org/10.1016/j.apsusc.2006.02.280)

42. B. Winterholler, P. Hoppe, M. O. Andreae, S. Foley, Measurement of sulfur isotope ratios in micrometer-sized samples by NanoSIMS. *Appl. Surf. Sci.* **252**, 7128 (2006).
[doi:10.1016/j.apsusc.2006.02.150](https://doi.org/10.1016/j.apsusc.2006.02.150)
43. B. Winterholler, P. Hoppe, S. Foley, M. O. Andreae, Sulfur isotope ratio measurements of individual sulfate particles by NanoSIMS. *Int. J. Mass Spectrom.* **272**, 63 (2008).
[doi:10.1016/j.ijms.2008.01.003](https://doi.org/10.1016/j.ijms.2008.01.003)
44. B. B. Demoz, J. L. Collett Jr., B. C. Daube Jr., On the Caltech Active Strand Cloudwater Collectors. *Atmos. Res.* **41**, 47 (1996). [doi:10.1016/0169-8095\(95\)00044-5](https://doi.org/10.1016/0169-8095(95)00044-5)
45. K. W. Fomba, K. Müller, D. van Pinxteren, H. Herrmann, Aerosol size-resolved trace metal composition in remote northern tropical Atlantic marine environment: case study Cape Verde Islands. *Atmos. Chem. Phys. Discuss.* **12**, 29535 (2012). [doi:10.5194/acpd-12-29535-2012](https://doi.org/10.5194/acpd-12-29535-2012)
46. K. F. Moore, D. E. Sherman, J. E. Reilly, J. L. Collett, Drop size-dependent chemical composition in clouds and fogs. Part I. Observations. *Atmos. Environ.* **38**, 1389 (2004).
[doi:10.1016/j.atmosenv.2003.12.013](https://doi.org/10.1016/j.atmosenv.2003.12.013)
47. K. F. Moore *et al.*, Drop size-dependent chemical composition of clouds and fogs. Part II: Relevance to interpreting the aerosol/trace gas/fog system. *Atmos. Environ.* **38**, 1403 (2004). [doi:10.1016/j.atmosenv.2003.12.014](https://doi.org/10.1016/j.atmosenv.2003.12.014)
48. H. Gerber, Direct measurement of suspended particulate volume concentration and far-infrared extinction coefficient with a laser-diffraction instrument. *Appl. Opt.* **30**, 4824 (1991). [doi:10.1364/AO.30.004824](https://doi.org/10.1364/AO.30.004824)
49. B. G. Arends *et al.*, Microphysics of clouds at Kleiner Feldberg. *J. Atmos. Chem.* **19**, 59 (1994). [doi:10.1007/BF00696583](https://doi.org/10.1007/BF00696583)
50. I. Trebs *et al.*, Real-time measurements of ammonia, acidic trace gases and water-soluble inorganic aerosol species at a rural site in the Amazon Basin. *Atmos. Chem. Phys.* **4**, 967 (2004). [doi:10.5194/acp-4-967-2004](https://doi.org/10.5194/acp-4-967-2004)
51. A. Mariotti *et al.*, Experimental determination of nitrogen kinetic isotope fractionation: Some principles; illustration for the denitrification and nitrification processes. *Plant Soil* **62**, 413 (1981). [doi:10.1007/BF02374138](https://doi.org/10.1007/BF02374138)

52. H. Krouse, V. Grinenko, Eds., *Stable Isotopes: Natural and Anthropogenic Sulphur in the Environment* (Wiley, Chichester, UK, 1991).
53. W. A. Tucker, L. H. Nelken, *Handbook of Chemical Property Estimation Methods* (American Chemical Society, Washington, DC, 1982), chap. 17.
54. M. Chin *et al.*, Atmospheric sulfur cycle simulated in the global model GOCART: Comparison with field observations and regional budgets. *J. Geophys. Res.* **105**, 24689 (2000). [doi:10.1029/2000JD900385](https://doi.org/10.1029/2000JD900385)
55. D. Thornton, A. Bandy, Sulfur dioxide and dimethyl sulfide in the central Pacific troposphere. *J. Atmos. Chem.* **17**, 1 (1993). [doi:10.1007/BF00699110](https://doi.org/10.1007/BF00699110)
56. D. Thornton, A. Bandy, B. Blomquist, D. Davis, R. W. Talbot, Sulfur dioxide as a source of condensation nuclei in the upper troposphere of the Pacific Ocean. *J. Geophys. Res.* **101**, 1883 (1996). [doi:10.1029/95JD02273](https://doi.org/10.1029/95JD02273)
57. B. W. Sinha, P. Hoppe, J. Huth, S. Foley, M. O. Andreae, Sulfur isotope analyses of individual aerosol particles in the urban aerosol at a central European site (Mainz, Germany). *Atmos. Chem. Phys.* **8**, 7217 (2008). [doi:10.5194/acp-8-7217-2008](https://doi.org/10.5194/acp-8-7217-2008)
58. U. Poschl *et al.*, Rainforest aerosols as biogenic nuclei of clouds and precipitation in the Amazon. *Science* **329**, 1513 (2010). [doi:10.1126/science.1191056](https://doi.org/10.1126/science.1191056)
59. Y. G. Zuo, J. Zhan, Effects of oxalate on Fe-catalyzed photooxidation of dissolved sulfur dioxide in atmospheric water. *Atmos. Environ.* **39**, 27 (2005). [doi:10.1016/j.atmosenv.2004.09.058](https://doi.org/10.1016/j.atmosenv.2004.09.058)
60. S. Cohen, S. G. Chang, S. S. Markowitz, T. Novakov, Role of fly ash in catalytic oxidation of sulfur(IV) slurries. *Environ. Sci. Technol.* **15**, 1498 (1981). [doi:10.1021/es00094a013](https://doi.org/10.1021/es00094a013)
61. N. Kaaden *et al.*, State of mixing, shape factor, number size distribution, and hygroscopic growth of the Saharan anthropogenic and mineral dust aerosol at Tinfou, Morocco. *Tellus B* **61**, 51 (2009). [doi:10.1111/j.1600-0889.2008.00388.x](https://doi.org/10.1111/j.1600-0889.2008.00388.x)
62. A. Kasper-Giebl, A. Koch, R. Hitzenberger, H. Puxbaum, *J. Atmos. Chem.* **35**, 33 (2000). [doi:10.1023/A:1006250508562](https://doi.org/10.1023/A:1006250508562)

63. H. Herrmann *et al.*, Towards a more detailed description of tropospheric aqueous phase organic chemistry: CAPRAM 3.0. *Atmos. Environ.* **39**, 4351 (2005).
[doi:10.1016/j.atmosenv.2005.02.016](https://doi.org/10.1016/j.atmosenv.2005.02.016)
64. C. Brandt, R. van Eldik, Transition metal-catalyzed oxidation of sulfur(IV) oxides. Atmospheric-relevant processes and mechanisms. *Chem. Rev.* **95**, 119 (1995).
[doi:10.1021/cr00033a006](https://doi.org/10.1021/cr00033a006)
65. R. K. Ulrich, G. T. Rochelle, R. E. Prada, Enhanced oxygen absorption into bisulphite solutions containing transition metal ion catalysts. *Chem. Eng. Sci.* **41**, 2183 (1986).
[doi:10.1016/0009-2509\(86\)87134-2](https://doi.org/10.1016/0009-2509(86)87134-2)
66. J. T. Jayne, P. Davidovits, D. R. Worsnop, M. S. Zahniser, C. E. Kolb, Uptake of sulfur dioxide(G) by aqueous surfaces as a function of pH: the effect of chemical reaction at the interface. *J. Phys. Chem.* **94**, 6041 (1990). [doi:10.1021/j100378a076](https://doi.org/10.1021/j100378a076)
67. B. Mayer, K. H. Feger, A. Giesemann, H.-J. Jäger, Interpretation of sulfur cycling in two catchments in the Black Forest (Germany) using stable sulfur and oxygen isotope data. *Biogeochemistry* **30**, 31 (1995). [doi:10.1007/BF02181039](https://doi.org/10.1007/BF02181039)
68. E. S. Saltzman, G. Brass, D. Price, The mechanism of sulfate aerosol formation: Chemical and sulfur isotopic evidence. *Geophys. Res. Lett.* **10**, 513 (1983).
[doi:10.1029/GL010i007p00513](https://doi.org/10.1029/GL010i007p00513)
69. H. Krouse *et al.*, in *Stable Isotopes: Natural and Anthropogenic Sulphur in the Environment*, H. Krouse, V. Grinenko, Eds. (Wiley, Chichester, UK, 1991), pp. 307–416.
70. K. M. Torfs, R. VanGrieken, F. Buzek, Use of stable isotope measurements to evaluate the origin of sulfur in gypsum layers on limestone buildings. *Environ. Sci. Technol.* **31**, 2650 (1997). [doi:10.1021/es970067v](https://doi.org/10.1021/es970067v)
71. M. Novák, I. Jackova, E. Prechova, Temporal trends in the isotope signature of air-borne sulfur in central Europe. *Environ. Sci. Technol.* **35**, 255 (2001). [doi:10.1021/es0000753](https://doi.org/10.1021/es0000753)
72. A. Kumar, M. M. Sarin, B. Srinivas, Aerosol iron solubility over Bay of Bengal: Role of anthropogenic sources and chemical processing. *Mar. Chem.* **121**, 167 (2010).
[doi:10.1016/j.marchem.2010.04.005](https://doi.org/10.1016/j.marchem.2010.04.005)

73. I.-C. Tsai, J.-P. Chen, P.-Y. Lin, W.-C. Wang, I. Isaksen, Sulfur cycle and sulfate radiative forcing simulated from a coupled global climate-chemistry model. *Atmos. Chem. Phys.* **10**, 3693 (2010). [doi:10.5194/acp-10-3693-2010](https://doi.org/10.5194/acp-10-3693-2010)
74. S. Wong, W.-C. Wang, I. Isaksen, T. Berntsen, J. Sundet, A global climate-chemistry model study of present-day tropospheric chemistry and radiative forcing from changes in tropospheric O₃ since the preindustrial period. *J. Geophys. Res.* **109**, D11309 (2004). [doi:10.1029/2003JD003998](https://doi.org/10.1029/2003JD003998)
75. M. Thomas *et al.*, Quantification of DMS aerosol-cloud-climate interactions using the ECHAM5-HAMMOZ model in a current climate scenario. *Atmos. Chem. Phys.* **10**, 7425 (2010). [doi:10.5194/acp-10-7425-2010](https://doi.org/10.5194/acp-10-7425-2010)
76. R. J. Park, D. J. Jacob, B. D. Field, R. M. Yantosca, M. Chin, Natural and transboundary pollution influences on sulfate-nitrate-ammonium aerosols in the United States: Implications for policy. *J. Geophys. Res.* **109**, D15204 (2004). [doi:10.1029/2003JD004473](https://doi.org/10.1029/2003JD004473)
77. S. Watanabe *et al.*, MIROC-ESM 2010: Model description and basic results of CMIP5-20c3m experiments. *Geosci. Model Dev.* **4**, 845 (2011). [doi:10.5194/gmd-4-845-2011](https://doi.org/10.5194/gmd-4-845-2011)
78. P. Rasch, M. Barth, J. Kiehl, S. Schwartz, C. Benkovitz, A description of the global sulfur cycle and its controlling processes in the National Center for Atmospheric Research Community Climate Model, Version 3. *J. Geophys. Res.* **105**, 1367 (2000). [doi:10.1029/1999JD900777](https://doi.org/10.1029/1999JD900777)
79. J. E. Kristjánsson, T. Iversen, A. Kirkevåg, Ø. Seland, J. Debernard, Response of the climate system to aerosol direct and indirect forcing: Role of cloud feedbacks. *J. Geophys. Res.* **110**, D24206 (2005). [doi:10.1029/2005JD006299](https://doi.org/10.1029/2005JD006299)
80. D. Spracklen, K. Pringle, K. Carslaw, M. Chipperfield, G. Mann, A global off-line model of size-resolved aerosol microphysics: I. Model development and prediction of aerosol properties. *Atmos. Chem. Phys.* **5**, 2227 (2005). [doi:10.5194/acp-5-2227-2005](https://doi.org/10.5194/acp-5-2227-2005)
81. H. Korhonen, K. Carslaw, D. Spracklen, G. Mann, M. Woodhouse, Influence of oceanic dimethyl sulfide emissions on cloud condensation nuclei concentrations and seasonality

- over the remote Southern Hemisphere oceans: A global model study. *J. Geophys. Res.* **113**, D15204 (2008). [doi:10.1029/2007JD009718](https://doi.org/10.1029/2007JD009718)
82. D. Koch, D. Jacob, I. Tegen, D. Rind, M. Chin, Tropospheric sulfur simulation and sulfate direct radiative forcing in the Goddard Institute for Space Studies general circulation model. *J. Geophys. Res.* **104**, 23799 (1999). [doi:10.1029/1999JD900248](https://doi.org/10.1029/1999JD900248)
83. P. J. Adams, J. H. Seinfeld, Predicting global aerosol size distributions in general circulation models. *J. Geophys. Res.* **107**, 4370 (2002). [doi:10.1029/2001JD001010](https://doi.org/10.1029/2001JD001010)
84. S. Menon, A. Del Genio, D. Koch, G. Tselioudis, GCM simulations of the aerosol indirect effect: Sensitivity to cloud parameterization and aerosol burden. *J. Atmos. Sci.* **59**, 692 (2002). [doi:10.1175/1520-0469\(2002\)059<0692:GSOTAI>2.0.CO;2](https://doi.org/10.1175/1520-0469(2002)059<0692:GSOTAI>2.0.CO;2)
85. M. Chin, R. B. Rood, S.-J. Lin, J.-F. Müller, A. M. Thompson, Atmospheric sulfur cycle simulated in the global model GOCART: Model description and global properties. *J. Geophys. Res.* **105**, 24671 (2000). [doi:10.1029/2000JD900384](https://doi.org/10.1029/2000JD900384)
86. L. C. Shaffrey *et al.*, U.K. HiGEM: The New U.K. High-Resolution Global Environment Model—Model description and basic evaluation. *J. Clim.* **22**, 1861 (2009). [doi:10.1175/2008JCLI2508.1](https://doi.org/10.1175/2008JCLI2508.1)
87. J.-L. Dufresne, J. Quaas, O. Boucher, S. Denvil, L. Fairhead, Contrasts in the effects on climate of anthropogenic sulfate aerosols between the 20th and the 21st century. *Geophys. Res. Lett.* **32**, L21703 (2005). [doi:10.1029/2005GL023619](https://doi.org/10.1029/2005GL023619)
88. C. Textor *et al.*, Analysis and quantification of the diversities of aerosol life cycles within AeroCom. *Atmos. Chem. Phys.* **6**, 1777 (2006). [doi:10.5194/acp-6-1777-2006](https://doi.org/10.5194/acp-6-1777-2006)
89. R. Sander, J. Lelieveld, P. J. Crutzen, Modelling of the nighttime nitrogen and sulfur chemistry in size resolved droplets of an orographic cloud. *J. Atmos. Chem.* **20**, 89 (1995). [doi:10.1007/BF01099920](https://doi.org/10.1007/BF01099920)